High-efficiency bidirectional resonant WPT system for electric vehicles

Marojahan Tampubolon[1], Huang-Jen Chiu[2], Hsin-Che Hsieh[3], Jing-Yuan Lin[2], Yao-Ching Hsieh[4]

[1]Department of Electrical Engineering, Faculty of Information and Technology, Universitas Multimedia Nusantara, Jakarta, Indonesia
[2]Department of Electronic and Computer Engineering, National Taiwan University of Science and Technology, Taipei, Taiwan
[3]Department of Electrical and Computer Engineering, Virginia Polytechnic Institute and State University, Blacksburg, United States
[4]Department of Electrical Engineering, College of Engineering, National Sun Yat-sen University, Kaoshiung, Taiwan

Article Info

ABSTRACT

The wireless power transfer (WPT) system has become popular given its safety and flexibility in electric vehicle (EVs) charging applications. Due to the increasing number of EVs, vehicle to grid (V2G) can be implemented in the future in which a bidirectional WPT is one of the key features. A high-efficiency bidirectional resonant WPT system is studied and implemented in this study. Besides bidirectional capability, single stage and regulated output voltage are other features of this work. It is done by using the variable frequency control without sacrificing efficiency and conforming to the typical frequency range of the WPT system for EVs application. The analysis of the series-series compensated WPT is presented, followed by the design consideration of the developed bidirectional WPT system. At last, the implementation and experimental results for a 3 kW laboratory prototype are also presented to show the validity and the feasibility of the proposed scheme. A 96.8% efficiency at a 210-mm gap and a 95% efficiency at a 250-mm gap can be achieved under a rated power condition.
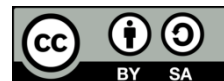
Corresponding Author:

Marojahan Tampubolon
Department of Electrical Engineering, Faculty of Information and Technology
Universitas Multimedia Nusantara
Scientia Boulevard, Kelapa Dua, Tangerang, Banten 15810, Indonesia
Email: marojahan.tampubolon@umn.ac.id

1. INTRODUCTION

Electric vehicles (EVs) have gained popularity worldwide among industrial and academic researchers. According to International Energy Agency Global EV Outlook 2022, EV stocks have increased significantly since 2010 from only hundreds to 16.5 million in 2021. IEA also projected the number of EVs to be around 200 million in 2030 using the stated policy scenario [1]. EVs have their batteries as the energy storage devices that need to be charged from the power system grid. In the meantime, it increases the proliferation of batteries that can be connected or disconnected from the power grid. During the charging period, a battery acts as the load, and the power grid acts as the power source. When a large number of batteries are charged simultaneously, the surge of load may disturb the power system's stability. Instead of treating the EVs battery only as a load to the power system, it is possible to use it as the energy storage device that can inject power into the system in a designated time. This system is called a vehicle-to-grid (V2G), as has been studied in [2]–[7]. The study in [2], [3] suggested that the V2G system has the potential to enhance grid stability and reliability and decrease the infrastructure cost of a large-scale renewable energy grid due to the storage devices distributed among users. Meanwhile, the researchers [4], [6] proposed the new model assessment of a radial distribution system with EVs load, and Mohamed and Hassan [5] studied V2G

model in micro grid using DC fast charging architecture. From the economic perspective, V2G system may allow EV owners to sell stored energy during off-peak periods in peak hours.

Battery charging systems can be classified into the plug-in and contactless charging systems. Plug-in charging systems, also known as conductive charging, use direct contact between the EV and charger inlet [8], [9]. This charging system has some disadvantages, including inflexibility and long charging time. Although a fast charging system may address the system's ineffectiveness, a battery with a large current capacity is needed, and a surge of the load of the grid system must be created. In addition to these problems, safety issues and range anxiety may cause consumers resistance to using EVs. A contactless charging system was introduced to solve these problem [10]. In addition to its safe and cordless system [11], [12], wireless power transfer (WPT) is unaffected by dirt, dust, water, and some chemicals [13]–[15].

A bidirectional charging system must be installed to enable the V2G or vehicle to home (V2H) system [16]. Considering the advantages of bidirectional WPT, a bidirectional WPT has been studied and implemented in [17]. The maximum efficiency obtained in this system was around 85%. However, the system's air gap is small (4 cm) and unsuitable for practical EV chargers. It also used a double-sided LCL compensation topology that added two compensation inductors. As a result, the cost, weight, and size are also increased. A system proposed in [18] implement a bidirectional power converter for multiple EVs, but the system use a plug-in method in their system. This paper aims to extend the study of the bidirectional WPT by implementing the series-series compensation to take advantage of its simplicity and lower components count. The contribution includes: i) The analysis and design of high-efficiency series-series compensated bidirectional WPT with a significantly more significant air gap and efficiency; and ii) The method to regulate the output voltage without using the pre-regulator or post regulator but only by using the variable frequency control. This paper section is arranged into an introduction followed by circuit analysis and design and control strategy in sections 2 and 3 consecutively. Section 4 presents a hardware and experimental verification results that includes discussions of results. At last, a conclusion is also provided.

2. CIRCUIT ANALYSIS

The circuit block shown in Figure 1 indicates that the WPT system has a symmetric topology at the primary (side A) and secondary (side B) sides. Each side consists of a full-bridge inverter, LC resonant compensator, coils, gate driver, digital controller, and RF feedback communication devices. The full-bridge inverter at side A converts the DC input voltage to square AC voltage for wireless power transfer through resonant compensator and coils. On the B side, the full-bridge circuit acts as a synchronous rectifier that produces the DC voltage to the load. A reversed process occurs under the reversed power flow. The coils are separated by a relatively large air gap, resulting in loosely magnetic coupled coils that can be modeled as a coupled inductor, as shown in Figure 2 [19]–[22].
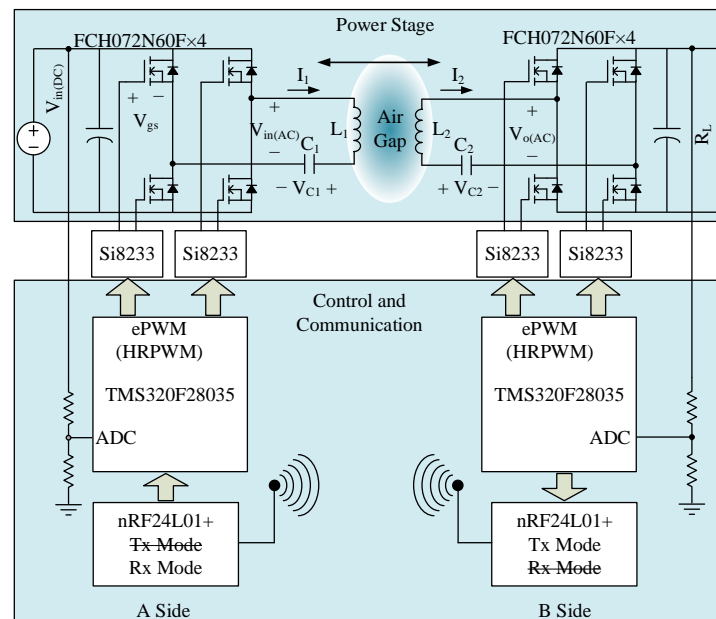

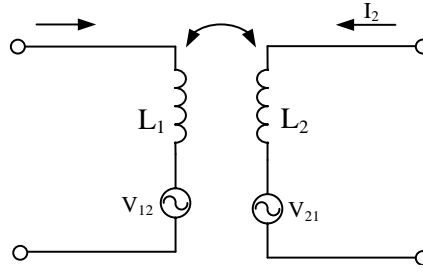Figure 1. Bidirectional series-series resonant WPT

Figure 2. Coupled inductor model

Primary current (I_1) induces the magnetic field to the secondary coil, generating the V_{21} voltage on the secondary side. I2 also generates the V21 voltage on the primary side with the same principle. The values of these voltages are dependent on the mutual inductance (M) of the coupled inductor as expressed in (1)-(3).

$$V_{12} = j\omega M I_2 \tag{1}$$

$$V_{21} = -j\omega M I_1 \tag{2}$$

$$M = k\sqrt{L_1 L_2} \tag{3}$$

A resonant compensation circuit is necessary to compensate for the low coupling coefficient of coils. There are four basic types of compensation that include series-series (SS), series-parallel (SP), parallel-series (PS), and parallel-parallel (PP) compensation [23]. This paper aims to develop a bidirectional WPT with identical behaviour for both power flow directions. Then, a symmetrical-SS compensator, as shown in Figure 1, was selected for this prototype because it is more suitable for voltage source converters than the parallel topology. In addition, it is also have a higher efficiency compared to parallel topology [24]. Let's assume that the B-side inverter works as a full bridge rectifier to simplify the analysis. Based on the first harmonic approximation, only the fundamental frequency is considered. The equivalent AC voltage $V_{in(AC)}$, generated by the FB inverter, is expressed as (4). The effective voltage is shown in (5) and the voltage transfer gain of the inverter in (6). The relationship between the output voltage of resonant compensator $V_{o(AC)}$ and DC output voltage $V_{o(DC)}$ across the bridge rectifier is a reversed inverter process, as shown in (7). By multiplying (6) and (7), a unity gain "1" is obtained. Therefore, the whole system's transfer function only depends on the resonant compensator and coils. All DC parameters are converted to the AC parameters. The voltage source is represented by the $V_{in(AC)}$, and DC load R_L is converted to equivalent AC load $R_{L(AC)}$. Then, the secondary impedance Z_s expressed in (9) are reflected into the primary side as reflected impedance Z_r. The input impedance of the system can be calculated by (10). By doing so, the simplified model can be redrawn, as shown in Figure 3.

$$V_{in(AC)} = \frac{4}{\pi} V_{in(DC)} sin(\omega t) \tag{4}$$

$$V_{in(AC),rms} = \frac{2\sqrt{2}}{\pi} V_{in(DC)} \tag{5}$$

$$G_{v(FB-inv)} = \frac{V_{in(AC),rms}}{V_{in(DC)}} = \frac{2\sqrt{2}}{\pi} \tag{6}$$

$$G_{v(FB-rect)} = \frac{V_o}{V_{o(AC),rms}} = \frac{\pi}{2\sqrt{2}} \tag{7}$$

$$R_{L(AC)} = \frac{8}{\pi^2} R_L \tag{8}$$

$$Z_s = j\omega L_2 + \frac{1}{j\omega C_2} + R_{L(AC)} \tag{9}$$

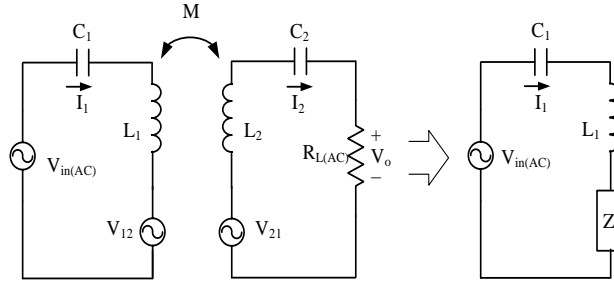$$Z_r = \frac{\omega^2 M}{Z_s} \tag{10}$$

Figure 3. Equivalent model of SS compensation WPT circuit

A transfer function has been derived and expressed in (12) to see the voltage gain characteristic. Figure 4 provides the plot of various equivalent AC loads and mutual inductance. We can select the random values to plot the voltage gain of the SS-WPT. In this case, parameters have been selected purposively using the calculated value in section 3 to avoid redundant plots in the next section. The parameters used are $C_1 = C_2 = 10$ nF, $L_1 = 437$ μH, and $L_2 = 442$ μH, and the equivalent AC output load $R_{L(AC)} = 53.33$ Ω. The various mutual inductances are used in the plot to see the impact of the coil's misalignment. From the plotted curves in Figure 4, it is clear that for any load and mutual inductance, there are always two unity gain load independent frequencies shown as ω_{L1} and ω_{H1} for $M = 89.2$ μH. The unity gain independent frequency derivation has been done in [25], and by assuming (13) is satisfied, the independent load frequencies can be calculated by using (14) and (15). It is clear from these equations that independent load frequencies are subjected to the coupling coefficient of the coils, as shown as ω_{L2}, ω_{H2}, ω_{L3}, and ω_{H3} in Figure 4.

$$Z_{in} = j\omega L_1 + \frac{1}{j\omega C_1} + Z_r = j\omega L_1 + \frac{1}{j\omega C_1} + \frac{\omega^2 M^2}{j\omega L_1 + \frac{1}{j\omega C_2} + R_{L(AC)}} \tag{11}$$

$$G_v = \left| \frac{V_o}{V_{in(DC)}} \right| = \frac{j\omega M R_{L(AC)}}{Z_s \left(j\omega L_1 + \frac{1}{j\omega C_1} \right) + \omega^2 M^2} \tag{12}$$

$$\omega = \frac{1}{\sqrt{L_1 C_1}} = \frac{1}{\sqrt{L_2 C_2}} \tag{13}$$

$$\omega_L = \frac{1}{\sqrt{(1+k)L_1 C_1}} \tag{14}$$

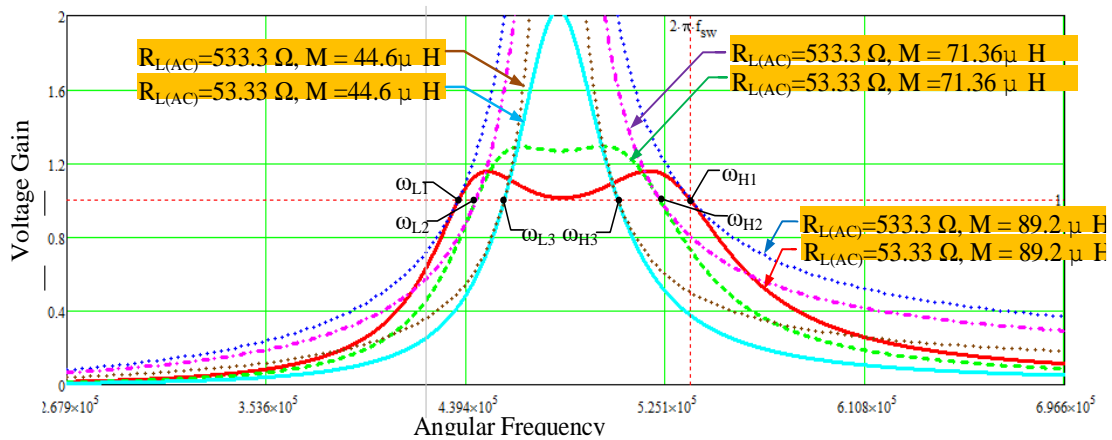$$\omega_H = \frac{1}{\sqrt{(1-k)L_1 C_1}} \tag{15}$$

Figure 4. Voltage gain plot of SS compensated WPT voltage gain with load and mutual inductance variation

3. DESIGN AND CONTROL STRATEGY

3.1. Operating frequency consideration

This paper proposes a single-stage regulated output voltage WPT in which the switching frequency is controlled to control the output voltage of the WPT converter. On the other hand, 81-91 kHz has been selected as the standard range of switching frequency of WPT for EV applications. This limitation must be satisfied while the voltage regulation can be maintained. According to the gain curve in Figure 4, the unity gain frequency exists at which the independent load variations can be achieved. This characteristic is desired because it will produce a more robust output voltage and less error fed to the controller in response to the large load variation. Operating at the independent load frequency results in the highest efficiency, and adjusting the switching frequency around the unity gain frequency does not reduce efficiency drastically. Therefore, limiting the frequency range around the unity gain is the best choice to implement this type of control. In this research, 85 kHz is the nominal frequency when the system operates in the full-load condition. Since two independent load frequencies exist, ω_L and ω_H, the designer has to decide in which area the system will be operated.

On the one hand, frequency ω_L is located in the capacitive area of the system. Therefore, achieving zero current switching (ZCS) in this area is possible. On the other hand, frequency ω_H is located in the inductive area at which the zero-voltage switching (ZVS) can be achieved. For this application, the operation MOSFET with ZVS is preferable. Therefore, the frequency ω_H is selected as the WPT's nominal operating frequency. Another concern about this operating frequency is the allowable misalignment of the system. As shown in Figure 4, the unity gain frequency moves proportionally to the mutual inductance variations. As a result, a limit of the allowable misalignment related to the minimum allowable coupling coefficient should be applied.

3.2. Efficiency consideration

The current flows in the A-side (I_1) can be calculated by combining (5) and (11), which are rewritten in (16). The same principle is also applied to solve the current on the B side.

$$I_{1,rms} = \frac{V_{in(AC),rms}}{|Z_{in}|} \tag{16}$$

$$I_{2,rms} = \frac{V_{o(AC),rms}}{R_{L(AC)}} \tag{17}$$

The power transferred from the transmitter to the receiver side is a crucial parameter in WPT technology. The coil's DC resistance (DCR) is larger than the MOSFET's conduction resistance. For this reason, the DCR of the transmitter (R_{L1}) and receiver (R_{L2}) sides are considered as pictured in Figure 5. The input impedance of the SS WPT is divided into two parts: reactance of the primary LC part X_1 and the reflected impedance Z_r. Therefore, all equations in the previous part related to the impedance should be modified with the correspondent location of the parameter. The power transferred from the transmitter to the receiver and the output power of the AC model is written in (18) and (19), respectively. Since the R_{L1} is considered, efficiency from the equivalent AC input, $V_{in(AC)}$, to the reflected impedance, Z_r, can be calculated with (20). Then the total efficiency of the AC model is expressed in (20). Figure 6 presents a plot of the power transferred and efficiency of the same hardware specification in sec. 2 with $R_{L1} = R_{L2} = 200$ mΩ for the various mutual inductances (top) and loads (bottom). We can see that the maximum efficiency is achieved when the WPT operates at the unity gain frequency. It is because, at this point, the circulating current is minimum.

$$P_{tr(A-B)} = I_1{}^2 \text{Re}(Z_r) = \frac{V_{in(AC),rms}}{|Z_{in}+R_{L1}|} \text{Re}\left(\frac{\omega^2 M^2}{Z_s+R_{L2}}\right) \tag{18}$$

$$P_{o(A-B)} = \left(\frac{G_v V_{in(AC),rms}}{R_{L(AC)}+R_{L2}}\right)^2 R_{L(AC)} \tag{19}$$

$$\eta_p = \frac{\text{Re}(Z_r)}{\text{Re}(Z_r)+R_{L1}} 100\%, \quad \eta_{tr} = \frac{P_{o(A-B)}}{P_{tr(A-B)}} 100\%, \quad then\ \eta = \eta_p x \eta_{tr} \tag{20}$$
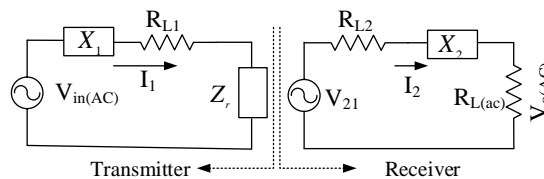

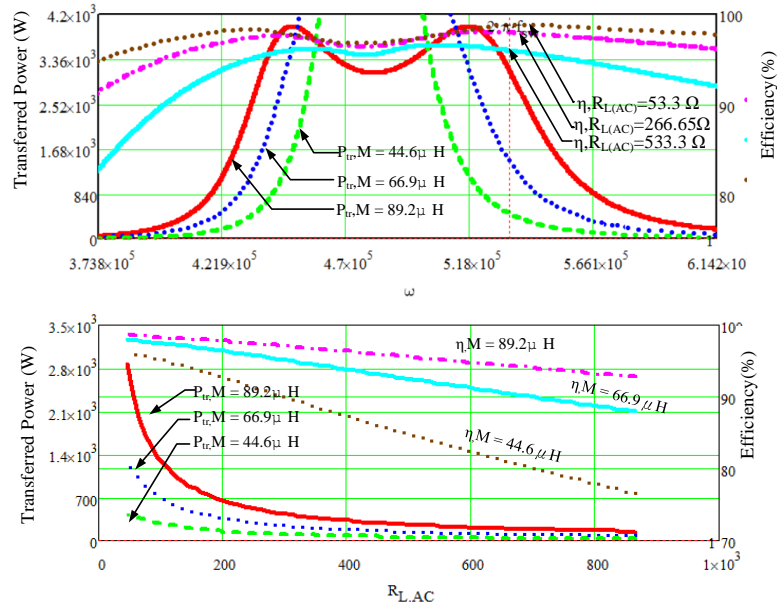Figure 5. The equivalent circuit includes DC resistance of coils

Figure 6. Transferred power and efficiency for various mutual inductances (M) and loads (RLAC)

Power losses must be analyzed and reduced to obtain a high-efficiency WPT system. Consider an SS resonant WPT works precisely at the resonant frequency. At this point, the impedance of the system has no imaginary component. Therefore, the WPT equivalent circuit only consists of the resistive loads and mutual inductance. It should be noted that the DC resistance of the coils and conduction resistance of the MOSFET are the primary sources of conduction loss. A larger imaginary impedance component in the system results in a larger circulating current that reduces the whole system's efficiency. Therefore, the switching frequency should not be too far from the resonant frequency to optimize the efficiency and power transfer of the WPT. Another approach for higher efficiency could be achieved by using a large coil inductance or increasing coupling coefficient k. However, the coupling coefficient depends on the coils dimension, allowable air gap, and allowable coil misalignment. The coil dimension and inductance determine the value of k. Using a larger inductance will increase the coupling coefficient. Thus, a large coil is necessary to increase efficiency. However, the coil's dimension, weight, and cost should be considered.

3.3. Resonant capacitor consideration

In SS WPT, resonant frequency and unity gain frequency are coincident. The unity gain frequency is dependent on the coupling coefficient. Figure 4 shows a plot of the voltage gain versus frequency for two coupling coefficient values and loads. The figure indicates that the unity gain frequency changes under various k. The selection of the resonant capacitor depends on the minimum operating frequency and the minimum allowable coupling coefficient. The minimum resonant capacitance of each side C_{xmin} of the circuit can be defined based on (21), where x is the symbol of the correspondent device either on the transmitter or on the receiver side. The resonant capacitor's voltage stress can be calculated using (22) and (23).

$$C_{xmin} = \frac{1}{\omega_{min}^2 (L_x - k_{min}\sqrt{L_1 L_2})} \tag{21}$$

$$V_{C1,max} = \frac{4}{\pi} \frac{V_{in(DC)}}{|Z_{in}|} \frac{1}{\omega C_1} \tag{22}$$

$$V_{C2,max} = \frac{4}{\pi} \frac{G_v \omega M}{R_{L(AC)}} \frac{1}{\omega C_2} \tag{23}$$

3.4. Control strategy

A control and communication block of the bidirectional WPT is depicted in Figure 7. The wireless communication uses nRF24L0+ single chip 2.4 GHz transceiver integrated with the DSP TMS320F28035. The ADC block of DSP senses the DC output voltage (Vo), and the output value is sent to the nRF24L0+ transmitter module to be received by the receiver module. The data communication between the modules is serial. The received data is processed and read as the controller's output voltage feedback (Vfb). A two pole

two zero (2P2Z) controller is employed to compensate for the output voltage error. Since the frequency range of the system is limited to 81-91 kHz, which is located in the inductive area of the curve, the behavior of the controller should be configured to increase the operating frequency when the output voltage is higher than the reference value and decrease when the output voltage is lower than the expected value. This control strategy allows the output voltage to be regulated to the desired value. The PWM period (T) should be updated every cycle to control the frequency.
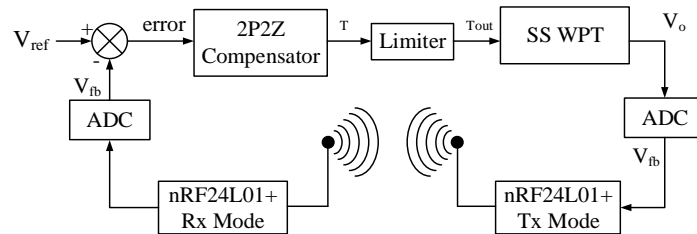
Figure 7. Control and communication strategy of proposed bidirectional WPT

4. HARDWARE AND EXPERIMENTAL VERIFICATION RESULTS
4.1. Hardware implementation

Table 1 shows the specifications of the developed SS-WPT system. Table 2 shows the specifications of the developed WPT system's identical transmitter and receiver coils. The Litz wire with size 0.1 mm × 600 is used to reduce the skin effect. Ferrite bars outside the coils increased the inductance and reduced flux leakage. As for capacitors, (21) was used to calculate the required capacitance, and the 10 nF thin-film capacitors were used as the compensator capacitors on the transmitter and receiver sides. For switching devices, FCH072N60F MOSFETs have been used on both sides of the inverter/rectifier. The developed transmitter and receiver are shown in Figure 8.
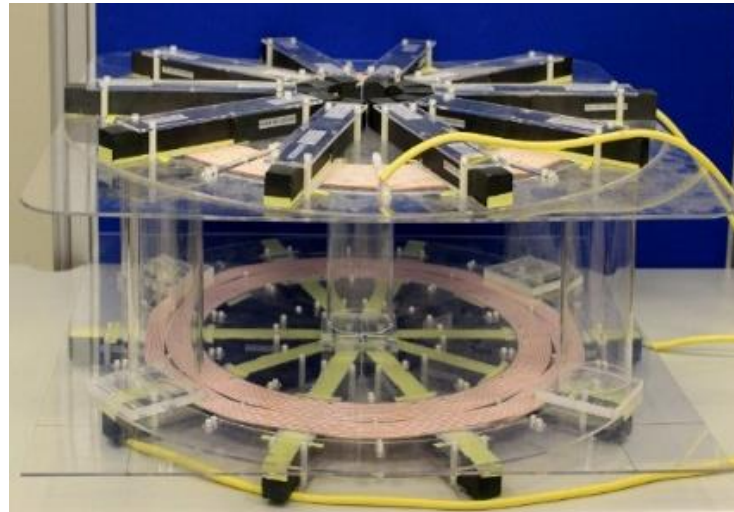
Figure 8. Transmitter and receiver coil of the proposed SS-WPT

Table 1. Specifications of series-series WPT system

Parameters	Value
Output power, P_o	3 kW
Input voltage, V_{in}	400 V
Output voltage, V_o	400 V
Coupling coefficient, k	0.15-0.25
Operating frequency, f_{sw}	81-91 kHz
Coil dimension	$\leqq$ 700×700 mm
Air gap	$\geqq$ 200 mm
Efficiency	$\geqq$ 95% @3kW

Table 2. Coil parameters and capacitor compensator of the WPT system

Parameters	Value	
Coil dimension (L×W)	700×700 cm	
Ferrite bar dimension (L×W×H)	150×26×26 mm	
Number of turns	20	
Coil separation distance	210 mm	250 mm
Self-inductance of side A, L_1	437 µH	434 µH
Self-inductance of side B, L_2	442 µH	439 µH
Coupling coefficient, k	0.203	0.151
Magnetizing inductance, L_m	89.2 µH	65.9 µH
Primary resonant capacitor, C_1	10 nF	
Secondary resonant capacitor, C_2	10 nF	

4.2. Experimental verification results

A 3 kW SS compensated WPT has been built to validate the analysis and design. Figure 9(a) presents the simulation waveforms of the WPT circuit under 300 W and Figure 9(b) presents the 3 kW output power. It shows the equivalent AC input and output voltage, resonant current, and voltage of the resonant capacitor. The simulated value agrees with the simulated value compared to the calculated value based on the given equation in the previous section. For instance, the I_1 current of the calculated and simulated value with 3 kW output power is 8.107 A and 8.18 A, respectively, and the maximum voltage in the capacitor, V_{C2}, is 2.24 kV calculated compared to 2.2 kV simulated. The ZVS simulated condition is also presented in Figure 9.
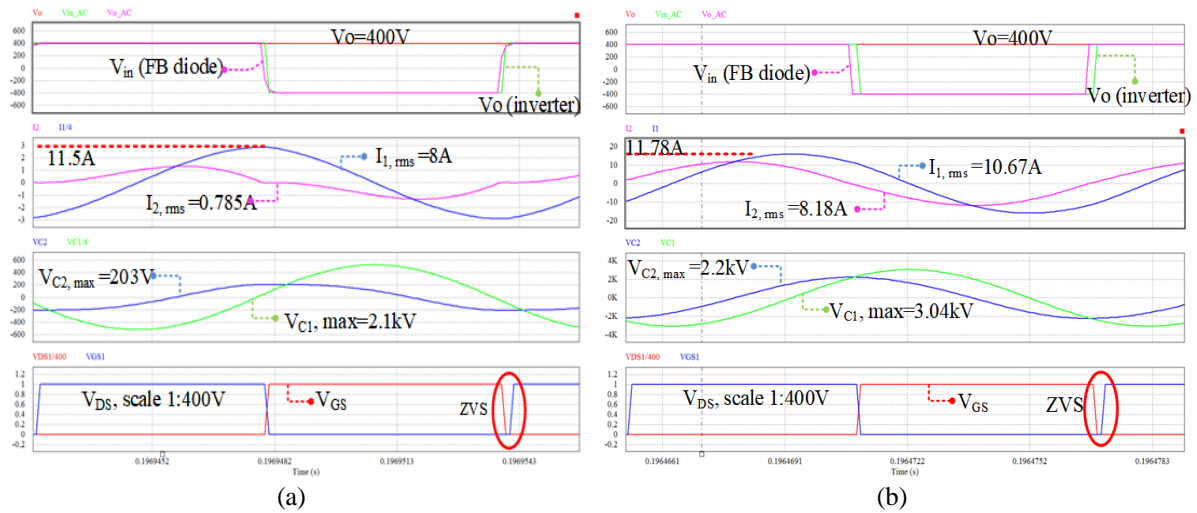
Figure 9. Simulated waveforms of the WPT circuit with M = 89.2 µH, (a) Po = 300 W and (b) Po = 3 kW

Figure 10 shows the experimental result of the SS WPT under 300 W and 3000 W output power with a 210 mm air gap. It provides the experimentally measured waveform of both sides which are Figure 10(a) for A side and Figure 10(b) for B side. Key waveforms for A side at 3 kW is shown in Figure 10(c) and for B side is shown in Figure 10(d). The ZVS condition also represented by Figures 10(e) and 10(f) for 300 W and 3 kW respectively. From this result, we can see the ZVS is achieved and 10% load and full load. The comparison between the calculated and experimental values is shown in Table 3. It has some differences because the calculation does not include all the parasitic parameters that affect the experimental result. For this reason, the difference between the calculated and measured results is considered acceptable. The experimental result for the 250 mm air gap is presented in Figure 11 in which Figures 11(a) and 11(b) show the key-waveforms for A and B side at 300 W output power respectively, followed by Figures 11(c)-11(d) at 3 kW output power. Figures 11(e)-11(f) show the ZVS condition at 300 W and 3 kW output power respectively. Since the mutual inductance of the coils decreases, the resonant current of both sides and the voltages stress of the capacitor are higher compared to the 210 mm air-gap results, which fit the theoretical analysis. The results also validate that the ZVS can be achieved under the smaller coupling coefficient.

All the presented waveforms are only for (A to B) power flow direction. The results for reversed direction are not included because the waveforms are identical. The measured efficiencies for bidirectional WPT are shown in Figure 12 (210-mm gap) and Figure 13 (250-mm gap). The experimental results indicate that the efficiency at the rated load condition can reach 96.4% and 96.8% at the 210-mm gap condition for the (A to B) and (B to A) power transfer directions, respectively. A slightly different result was also obtained by changing the power transfer direction because the coil parameters may vary. At the 250-mm gap condition, the measured efficiency can reach 95.1% and 95.4% for the (A to B) and (B to A) power transfer direction, respectively. The efficiency slightly decreases for a large coil separation because of the lower coupling coefficient that results in the lower magnetic inductance. A lower efficiency occurred at the small output power related to the large circulating current that increases the conduction loss of the WPT.

Table 3. Calculated and measured parameter of SS WPT with 210 mm air-gap

Parameter	Unit	Calculated	Measured	Calculated	Measured
Power	W	300		3000	
$I_{1,rms}$	A	7.85	7.58	11.65	10.50
$I_{2,rms}$	A	0.86	0.94	8.52	8.39
$V_{C1, max}$	kV	2.08	1.90	3.08	2.77
$V_{C2, max}$	kV	227.49	263.04	2.24	2.32
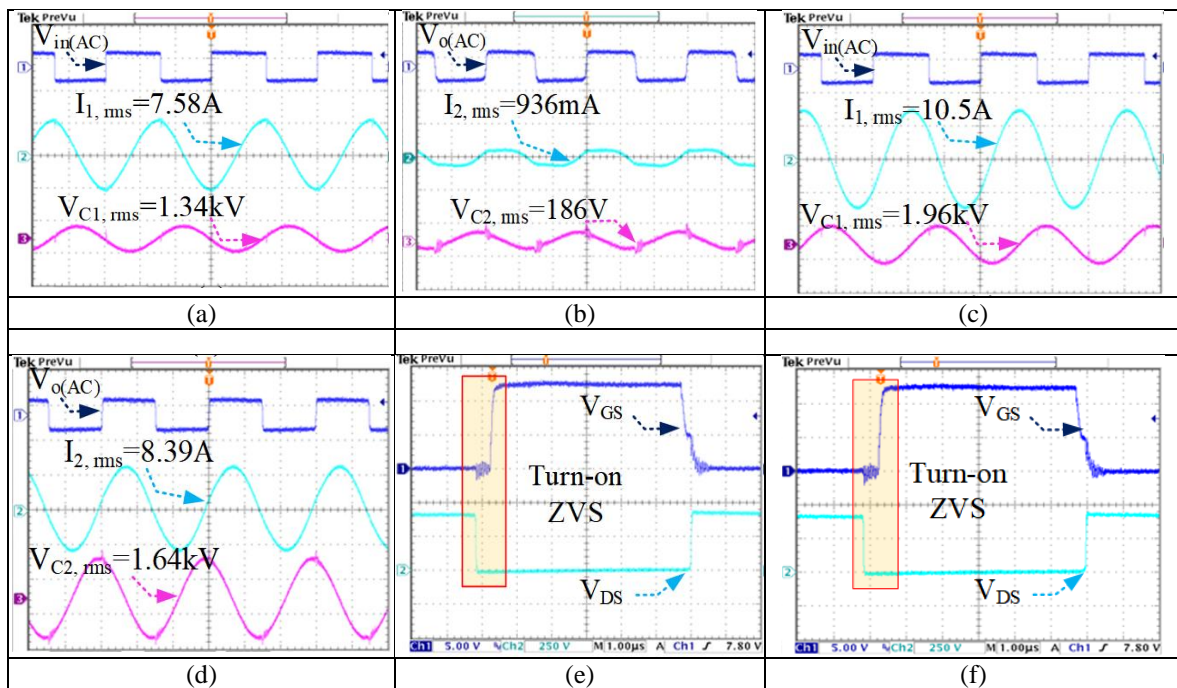
Figure 10. Key resonant waveforms of WPT circuit with 210-mm air gap (a) side A key-waveforms at Po = 300 W, (b) side B key-waveforms at Po = 300 W, (c) side A key-waveforms at Po = 3 kW, (d) side B key-waveforms at Po = 3 kW, (e) ZVS condition at Po = 300 W, and (f) ZVS condition at Po = 3 kW

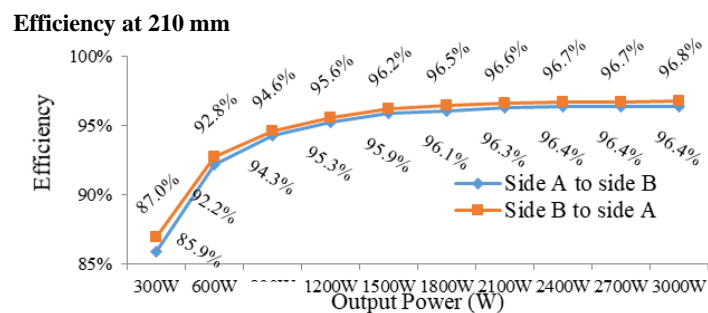Figure 12. Measured efficiency of the bidirectional WPT prototype at 210-mm air-gap
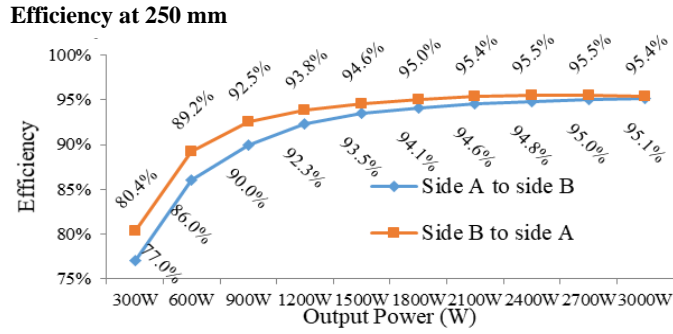
Efficiency at 250 mm

Figure 13. Measured efficiency of the bidirectional WPT prototype at 250-mm air-gap

5. CONCLUSION

A bidirectional WPT is necessary to enable a V2G system in the future. The SS-compensated resonant WPT circuit has been discussed in this paper, including detailed system analysis, design considerations, and experimental results. Variable frequency control was implemented instead of using a post-regulator stage. The SS resonant WPT prototype was successfully developed and tested to validate the proposed approach. The results showed that the bidirectional power flow could be achieved with an identic performance for both power flows. The ZVS can be performed either at the small or full loads condition. It also fulfils the efficiency target of beyond 95%. The maximum efficiency was 96.8% at a 210-mm coil separation with power flow direction from B to A. The efficiency also slightly decreased for a large coil separation and slightly differed for varying power flow directions. The successful implementation of the system verified that the analysis and the design procedure provided to design a high-efficiency series-series compensated bidirectional WPT are valid. The variable frequency control proposed to regulate the output voltage was also adequate and can be used in the WPT system. However, room for improvement is still required for the small load's efficiency in the future.

APPENDIX
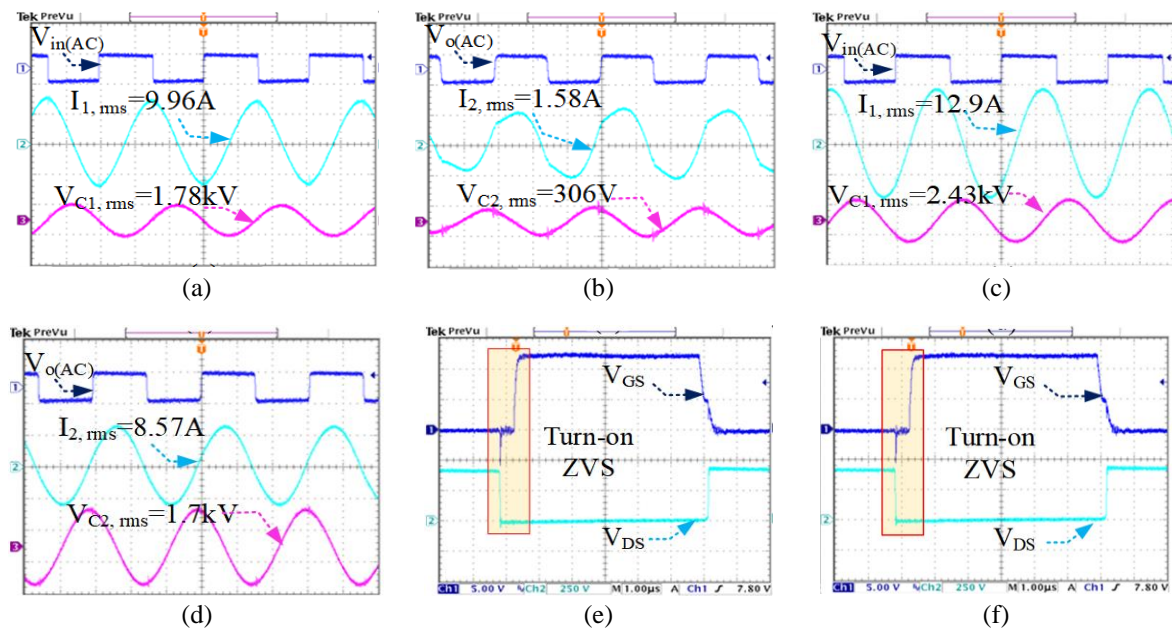
Figure 11. Key resonant waveforms of WPT circuit with 250-mm air gap (a) side A key-waveforms at Po = 300 W, (b) side B key-waveforms at Po = 300 W, (c) side A key-waveforms at Po = 3 kW, (d) side B key-waveforms at Po = 3 kW, (e) ZVS condition at Po = 300 W, and (f) ZVS condition at Po = 3 kW

REFERENCES

[1]   IEA, "Global electric vehicle outlook 2022," *International Energy Agency*, 2022. https://www.iea.org/reports/global-ev-outlook-2022.

[2]   Y. Ma, T. Houghton, A. Cruden, and D. Infield, "Modeling the benefits of vehicle-to-grid technology to a power system," *IEEE Transactions on Power Systems*, vol. 27, no. 2, pp. 1012–1020, May 2012, doi: 10.1109/TPWRS.2011.2178043.

[3]   W. Shuai, P. Maille, and A. Pelov, "Exploiting electric vehicles mobility to reduce grid dependency in transit areas," in *2016 IEEE International Energy Conference (ENERGYCON)*, Apr. 2016, pp. 1–6, doi: 10.1109/ENERGYCON.2016.7513999.

[4]   J. C. Hernández, F. J. Ruiz-Rodriguez, and F. Jurado, "Modelling and assessment of the combined technical impact of electric vehicles and photovoltaic generation in radial distribution systems," *Energy*, vol. 141, pp. 316–332, Dec. 2017, doi: 10.1016/j.energy.2017.09.025.

[5]   T. H. Mohamed and H. A. Hassan, "Terminal voltage and power regulation using vehicle-to-grid (V2G) schemes connected to a two-area power system," in *2018 Twentieth International Middle East Power Systems Conference (MEPCON)*, Dec. 2018, pp. 203–208, doi: 10.1109/MEPCON.2018.8635159.

[6]   F. J. Ruiz-Rodriguez, J. C. Hernández, and F. Jurado, "Voltage behaviour in radial distribution systems under the uncertainties of photovoltaic systems and electric vehicle charging loads," *International Transactions on Electrical Energy Systems*, vol. 28, no. 2, p. e2490, Feb. 2018, doi: 10.1002/etep.2490.

[7]   F. M. Shakeel and O. P. Malik, "Vehicle-to-grid technology in a micro-grid using DC fast charging architecture," in *2019 IEEE Canadian Conference of Electrical and Computer Engineering (CCECE)*, May 2019, pp. 1–4, doi: 10.1109/CCECE.2019.8861592.

[8]   K. W. Klontz, A. Esser, R. R. Bacon, D. M. Divan, D. W. Novotny, and R. D. Lorenz, "An electric vehicle charging system with 'universal' inductive interface," in *Proceedings of Power Conversion Conference - Yokohama 1993*, 1993, pp. 227–232, doi: 10.1109/PCCON.1993.264219.

[9]   A. Hassoune, M. Khafallah, A. Mesbahi, A. Nouaiti, and T. Bouragba, "Experimental implementation of a smart battery charger for electric vehicles charging station," *International Journal of Power Electronics and Drive Systems*, vol. 11, no. 4, pp. 1689–1699, Dec. 2020, doi: 10.11591/ijpeds.v11.i4.pp1689-1699.

[10] K. W. Klontz, D. M. Divan, D. W. Novotny, and R. D. Lorenz, "Contactless battery charging system," 1994. https://www.google.com/patents/US5341083.

[11] A. Mahesh, B. Chokkalingam, and L. Mihet-Popa, "Inductive wireless power transfer charging for electric vehicles–a review," *IEEE Access*, vol. 9, pp. 137667–137713, 2021, doi: 10.1109/ACCESS.2021.3116678.

[12] C.-S. Wang, O. H. Stielau, and G. A. Covic, "Design considerations for a contactless electric vehicle battery charger," *IEEE Transactions on Industrial Electronics*, vol. 52, no. 5, pp. 1308–1314, Oct. 2005, doi: 10.1109/TIE.2005.855672.

[13] J. T. Boys, G. A. Covic, and A. W. Green, "Stability and control of inductively coupled power transfer systems," *IEE Proceedings: Electric Power Applications*, vol. 147, no. 1, pp. 37–42, 2000, doi: 10.1049/ip-epa:20000017.

[14] G. A. Covic and J. T. Boys, "Modern trends in inductive power transfer for transportation applications," *IEEE Journal of Emerging and Selected Topics in Power Electronics*, vol. 1, no. 1, pp. 28–41, Mar. 2013, doi: 10.1109/JESTPE.2013.2264473.

[15] A. W. Green and J. T. Boys, "10 kHz inductively coupled power transfer - concept and control," in *IEE Conference Publication*, 1994, vol. 399, pp. 694–699, doi: 10.1049/cp:19941049.

[16] H. Shin and R. Baldick, "Plug-in electric vehicle to home (V2H) operation under a grid outage," *IEEE Transactions on Smart Grid*, vol. 8, no. 4, pp. 2032–2041, Jul. 2017, doi: 10.1109/TSG.2016.2603502.

[17] U. K. Madawala and D. J. Thrimawithana, "A bidirectional inductive power interface for electric vehicles in V2G systems," *IEEE Transactions on Industrial Electronics*, vol. 58, no. 10, pp. 4789–4796, Oct. 2011, doi: 10.1109/TIE.2011.2114312.

[18] A. D. Savio and V. J. A., "Development of multiple plug-in electric vehicle mobile charging station using bidirectional converter," *International Journal of Power Electronics and Drive Systems (IJPEDS)*, vol. 11, no. 2, pp. 785–791, Jun. 2020, doi: 10.11591/ijpeds.v11.i2.pp785-791.

[19] S. Li and C. C. Mi, "Wireless power transfer for electric vehicle applications," *IEEE Journal of Emerging and Selected Topics in Power Electronics*, vol. 3, no. 1, pp. 4–17, Mar. 2015, doi: 10.1109/JESTPE.2014.2319453.

[20] M. Ryu, H. Cha, Y. Park, and J. Back, "Analysis of the contactless power transfer system using modelling and analysis of the contactless transformer," in *31st Annual Conference of IEEE Industrial Electronics Society, 2005. IECON 2005.*, 2005, p. 7, doi: 10.1109/IECON.2005.1569047.

[21] C. Zheng *et al.*, "High-efficiency contactless power transfer system for electric vehicle battery charging application," *IEEE Journal of Emerging and Selected Topics in Power Electronics*, vol. 3, no. 1, pp. 65–74, Mar. 2015, doi: 10.1109/JESTPE.2014.2339279.

[22] F. Musavi and W. Eberle, "Overview of wireless power transfer technologies for electric vehicle battery charging," *IET Power Electronics*, vol. 7, no. 1, pp. 60–66, Jan. 2014, doi: 10.1049/iet-pel.2013.0047.

[23] Y. Zhang, S. Chen, X. Li, and Y. Tang, "Design of high-power static wireless power transfer via magnetic induction: an overview," *CPSS Transactions on Power Electronics and Applications*, vol. 6, no. 4, pp. 281–297, Dec. 2021, doi: 10.24295/cpsstpea.2021.00027.

[24] M. Rehman, P. Nallagownden, and Z. Baharudin, "Efficiency investigation of SS and SP compensation topologies for wireless power transfer," *International Journal of Power Electronics and Drive Systems (IJPEDS)*, vol. 10, no. 4, pp. 2157–2164, Dec. 2019, doi: 10.11591/ijpeds.v10.i4.pp2157-2164.

[25] Q. Chen, S. C. Wong, C. K. Tse, and X. Ruan, "Analysis, design and control of a transcutaneous power regulator for artificial heart," in *2008 IEEE Power Electronics Specialists Conference*, Jun. 2008, pp. 1833–1838, doi: 10.1109/PESC.2008.4592210.

BIOGRAPHIES OF AUTHORS

Marojahan Tampubolon [ID] [icons] is a lecturer in Electrical Engineering Department at the Universitas Multimedia Nusantara (UMN), Tangerang, Indonesia. He received his B.Eng. degree from the University of Sumatera Utara in 2009 and his M.Eng. and Ph.D. in Electronic Engineering from the National Taiwan University of Science and Technology in 2014 and 2018, respectively. He was with Vanguard International Semiconductor Corp. from 2018 to 2020. His research interest includes switching power converter, wireless power transfer, and renewable energy. He can be contacted at email: marojahantampubolon@umn.ac.id.

Huang-Jen Chiu [ID] [SC] is a Distinguished Professor and the Director of the Center for Power Electronic Technologies, Department of Electronic and Computer Engineering, NTUST, where he is also the Dean of Industry-Academia Collaboration with NTUST. He received his B.E. and Ph.D. degrees in electronic engineering from the National Taiwan University of Science and Technology (NTUST), Taipei City, Taiwan, in 1996 and 2000, respectively. He is currently a senior member of IEEE and a Fellow of the Institute of Engineering and Technology (IET). He was a Distinguished Lecturer of the IEEE Power Electronics Society from 2017 to 2018 and from 2019 to 2020. He was a recipient of several distinguished awards, including the Young Researcher Award from the Ministry of Science and Technology, Taiwan, in 2004, the outstanding teaching awards from NTUST in 2009 and 2017, and the Excellent Research Award from NTUST in 2009 and 2011. He was the Chair/Co-Chair of several international conferences, such as the IEEE International Future Energy Electronics Conference (IFEEC). He is also an Associate Editor of the IEEE Transactions on Industry Applications and IEEE Transactions on Circuits and Systems Part II: Express Letters (TCAS-II). He can be contacted at email: hjchiu@mail.ntust.edu.tw.

Hsin-Che Hsieh [ID] [SC] is a Ph.D. student at the Bradley Department of Electrical and Computer Engineering, Virginia Polytechnic Institute and State University, Blacksburg, VA, USA. He received his B.S. and M.S. degrees in electronic and computer engineering from the National Taiwan University of Science and Technology (Taiwan Tech), Taipei, Taiwan, in 2014 and 2016, respectively. His research interests include resonant power converters and wireless power transfer technology. He can be contacted at email: hchsieh@vt.edu.

Jing-Yuan Lin [ID] [SC] is an Associate Professor in the Department of Electronic and Computer Engineering, National Taiwan University of Science and Technology. He received his M.S. and Ph.D. degrees in electronic engineering from the National Taiwan University of Science and Technology, Taipei, Taiwan, in 2002 and 2007, respectively. His research interests include the design and analysis of zero-voltage-switching DC/DC converters, power factor correction, inverter techniques, converter modeling, and power IC design. He can be contacted at email: jylin@mail.ntust.edu.tw.

Yao-Ching Hsieh [ID] [SC] is an Associate Professor in the Department of Electrical Engineering, National Sun Yat-sen University, Kaohsiung, Taiwan. He received the B.E. and M.S. degrees from National Taiwan University, Taipei, Taiwan, in 1991 and 1993, respectively, and the Ph.D. degree from National Sun Yat-sen University in 2004, all in electrical engineering. From 2006 to 2014, he was with the Department of Electrical Engineering, National Dong Hwa University, Hualien, Taiwan. From 2014 to 2017, he was with the Department of Electronic and Computer Engineering, National Taiwan University of Science and Technology, Taipei. His research interests include battery-related technology, soft-switching techniques, and power converters. He can be contacted at email: ychsieh@mail.ee.nsysu.edu.tw.